Applied Energy 108 (2013) 466–476

Contents lists available at SciVerse ScienceDirect

Applied Energy

journal homepage: www.elsevier.com/locate/apenergy

Dynamic simulation of thermal-lag Stirling engines

Chin-Hsiang Cheng [a,b,*], Hang-Suin Yang [a,b], Bing-Yi Jhou [a,b], Yi-Cheng Chen [c], Yu-Jen Wang [c]

[a] Institute of Aeronautics and Astronautics, National Cheng Kung University, Taiwan
[b] Center for Micro/Nano Science and Technology, National Cheng Kung University, Taiwan
[c] Microsystems Technology Center, Industrial Technology Research Institute, Taiwan

HIGHLIGHTS

- First paper dealing with numerical dynamic simulation of thermal-lag Stirling engine.
- Observation on different operating modes, such as rotating, swinging, swinging-to-rotate, and swinging-to-decay modes.
- Study of influential factors affecting the operating modes.
- Optimal geometrical or operating parameters of the baseline case for maximum engine power are found.

ARTICLE INFO

Article history:
Received 15 November 2012
Received in revised form 15 March 2013
Accepted 24 March 2013
Available online 18 April 2013

Keywords:
Dynamic simulation
Thermal-lag Stirling engine
Shaft power
Brake thermal efficiency

ABSTRACT

The present study is concerned with dynamic simulation of thermal-lag Stirling engines. A dynamic model is built and incorporated with a thermodynamic model to study the engine start process. A prototype engine is designed and simulated by using the dynamic model. In the simulation, different operating modes, including rotating mode, swinging mode, swinging-to-rotate mode, and swinging-to-decay mode, have been observed. The rotating mode is desired and can be achieved if the operating parameters are properly designed. In a poor design, the engine may switch to the swinging or even the swinging-to-decay mode. In addition, it is found that geometric parameters, such as bore size, stroke, and volume of working spaces, also determine the operating mode of the engine. Brake thermal efficiency of the engine is monotonically reduced by increasing engine speed. However, study of the dependence of the shaft power of the engine speed shows that there exists a maximum value of the shaft power at an optimal operating engine speed. The optimal engine speed leading to maximum shaft power is significantly influenced by the geometrical parameters.

© 2013 Elsevier Ltd. All rights reserved.

1. Introduction

Among the promising renewable energy technologies, dish concentrating solar power (DCSP) systems have received increasing attention from the researchers in recent years. The DCSP system uses a dish to concentrate a large area of sunlight or solar thermal energy onto a small area. Electrical power is produced when the concentrated sunlight is converted to high-temperature thermal energy to drive a Stirling engine that is connected to an electrical power generator [1–3]. Besides, Stirling engine can also use natural gas or gasoline as auxiliary heat source so that it may still delivery power whenever the sunlight is not available. In some other cases, the engine is applied as a micro combined heat and power generation (micro-CHP) unit [4,5] that can supply both residential hot water and electricity.

Earlier technological development in the Stirling engines was reviewed by Thombare and Verma [6]. Traditionally, Stirling engines are categorized into three types namely, α-, β- and γ-types, in terms of the arrangement of pistons, displacers, and cylinders. In the three types of engines, typically an engine is equipped with at least two moving parts, a piston plus a displacer or another piston, in the cylinders. Relative movement between the two moving parts inside the cylinders is so carefully designed by assigning a phase angle between the two moving parts that the working fluid is able to flow back-and-forth between the heating and the cooling parts of the engine to absorb or reject heat, respectively, and then complete a thermodynamic cycle. Cheng and Yang [7] discussed the major differences in the configurations among the three types of engines and investigated relative performance of them. Rochelle and Grosu [8] took into consideration effects of exo-irreversibility and imperfect regeneration in the Schmidt model and obtained analytical solutions for engine speed, power and efficiency for different types of Stirling engine.

In 1979, Ceperley [9] presented a pistonless thermoacoustic Stirling engine which was demonstrated by using a looped tube

* Corresponding author. Address: Institute of Aeronautics and Astronautics, National Cheng Kung University, No. 1, Ta-Shieh Road, Tainan 70101, Taiwan, ROC. Tel.: +886 6 2757575x63627; fax: +886 6 2389940.
E-mail address: chcheng@mail.ncku.edu.tw (C.-H. Cheng).

0306-2619/$ - see front matter © 2013 Elsevier Ltd. All rights reserved.
http://dx.doi.org/10.1016/j.apenergy.2013.03.062

Nomenclature

$\vec{a}_A, \vec{a}_P$	acceleration of joints A and P (m/s^2)
a_{Py}	y component of $\vec{a}_P$ (m/s^2)
a_{PAcgx}, a_{PAcgy}	x and y components of acceleration of center of gravity of link PA (m/s^2)
$\vec{AP}$	vector (m)
A_r	cross section void area of regenerative heater (m^2)
c_p	constant pressure specific heat (J/kg K)
c_v	constant volume specific heat (J/kg K)
d_p	diameter of working space and piston (bore size) (m)
D_h	hydraulic diameter of regenerative channel (m)
e_x, e_y	components of vector AP (m)
f	Fanning friction factor
f_{gt}, f_{tg}	direction factor
F_{Ax}, F_{Ay}, F_{Px}, F_{Py}	x and y components of forces acting on joints A and P (N)
F_f	friction force at interface between piston and cylinder (N)
G	acceleration of gravity (m/s^2)
h_r	heat transfer coefficient of regenerative heater (W/m^2 K)
I_f, I_{PA}	moment of inertia of flywheel and link PA (kg m^2)
$\vec{i}, \vec{j}, \vec{k}$	unit vectors in Cartesian coordinate
k	conductivity of working fluid (W/m K)
K_f	empirical coefficient in relation between velocity and pressure drop
l_{PA}, l_r	length of link PA and regenerative heater (m)
m_g, m_t	mass of working fluid in gas chamber and thermal buffer chamber (kg)
m_p, m_{PA}	mass of piston and link PA (kg)
Nu	Nusselt number in regenerative heater
$\vec{OA}$	vector (m)
p_b, p_g, p_t	pressure in buffer, gas, and thermal buffer chambers (Pa)
p_0, p_{b0}	charged pressure in working space and buffer chamber (Pa)
P	perimeter of regenerative heater channel (m)
$\dot{Q}_{in}$	total heat input rate (W)
$\dot{Q}_{in,g}, \dot{Q}_{in,r}, \dot{Q}_{in,t}$	rate of heat transfer in gas chamber, regenerative heater, and thermal buffer chamber (W)
r	offset distance from crank to shaft center (m)
R	gas constant (J/K mol)
Re	Reynolds number of flow through regenerative heater
R_c, R_g, R_t	thermal resistance in compression chamber, gas chamber, and thermal buffer chamber (K/W)
R_l	total thermal resistance in cold side (K/W)
s	coefficient in Eq. (18) (m^{-1})
t	time (s)
T	temperature of working fluid through regenerative heater (K)
T_g, T_t	temperature of working fluid in gas chamber and thermal buffer chamber (K)
T'_g, T'_t	temperature of working fluid at outlet of regenerative heater in gas chamber and thermal buffer chamber (K)
T_{wg}, T_{wt}	wall temperatures of gas chamber and thermal buffer chamber (K)
T_{wr}	temperature of regenerative porous matrix (K)
$\bar{u}$	average velocity of working fluid through regenerative heater (m/s)
$\vec{v}_A, \vec{v}_P$	velocity of joints A and P (m/s)
v_{Py}	y components of $\vec{v}_P$ (m/s)
V_c, V_g, V_t	volume of compression chamber, gas chamber, and thermal buffer chamber (m^3)
$\dot{W}_i, \dot{W}_s$	indicated power and shaft power (W)

Greek symbols

γ	c_p/c_v
Γ_f, Γ_O	torque due to friction force and working gas pressure (N m)
Γ_{load}	loading torque (N m)
η_t, η_m, η_b	thermal, mechanical, and brake thermal efficiencies
μ	dynamic viscosity of working fluid (N s/m^2)
μ_p	coefficient of kinetic friction
ϕ	crank angle (rad)
ρ_{tg}	density of working fluid through regenerative heater (kg/m^3)
τ	period (s)
ω_O, ω_{PA}	angular velocity of flywheel and link PA (rad/s)
ω_{ave}	average angular velocity of flywheel (rad/s)
$\dot{\omega}_O, \dot{\omega}_{PA}$	angular acceleration of flywheel and link PA (rad/s^2)

Superscripts

0	initial
k	time step

with a differentially heated regenerator. The prototype engine with no moving piston revealed a concept that the traveling-wave thermoacoustic oscillations can be regarded as a kind of heat engine. Lately, Swift [10,11] and Swift and Garrett [12] found that the thermoacoustic concepts could be equally applicable to some reciprocating heat engines. Hamaguchi et al. [13] developed a simple engine called "pulse tube engine", which is equipped with one single reciprocating piston and does not utilize the natural frequency as in the thermoacoustic Stirling engines. Yoshida et al. [14] measured work flux density distribution over the cross section of the pulse tube to elucidate the work source of the engine. They found that the pulse tube engine belongs to the standing wave engine group and the work source resides not in the porous stack but in the pulse tube.

On the other hand, one other concept of the Stirling engine was proposed by Chen and West [15] and the engine was entitled "thermal-lag Stirling engine" afterward. The thermal-lag Stirling engine requires no displacer and its connected link, and instead, a porous-medium stack is fixed in the cylinder as a static regenerative heater. The first prototype of the thermal-lag engine and its performance testing were made by Tailer [16,17]. He stated that the engine experiences imperfect cooling and heating processes in the working spaces, and the imperfect cooling and heating cause a time lag in the gas temperature response as following the movement of the piston. Thus, the engine was named "thermal-lag" engine. A numerical model for the thermal-lag engine was proposed by Arques [18]. In this report, it could be observed that the areas of the thermodynamic cycles of the thermal-lag engine plotted in the p–V diagrams are rather small. It seemingly implies that that the thermal-lag engines are not capable of producing appreciable work output. Recently, Cheng and Yang [19] made a prototype thermal-lag engine of 15 W and also developed a thermodynamic model for predicting transient variations of the thermodynamic properties in the individual working spaces of the engine. Effects of geometrical and operating parameters, such as heating and cooling temperatures, volumes of the chambers, thermal resistances, stroke of piston, and bore size on indicated power output and thermal efficiency were also evaluated.

Similar to the pulse-tube engine, the thermal-lag engine has only one moving part (piston) and a static part (regenerative

heater) without the displacer and its link. As a matter of fact, the thermal-lag engine is frequently referred to as a special kind of the pulse tube engines. However, a standard pulse tube engine consists of a piston in one cylinder, a pulse tube, an orifice, a heater, a regenerator, a cooler and a second cooler, and a buffer zone [10–14], whereas the mechanism of the prototype of the thermal-lag engine presented by Tailer [16,17] does not include the pulse tube, the orifice, the second cooler, and the buffer zone so that its mechanical structure can be further simplified. Due to its simplicity in structure, its cost in manufacturing and maintenance can relatively low. Besides, it has been observed from the experiments on the prototype engine made by Cheng and Yang [19] that the engine can be slightly pushed to start. When a small initial rotation speed is applied, the engine starts with a bi-directional swinging mode in a short period of time and then proceeds to a uni-directional rotating mode. This can be called "swinging-to-rotate" mode. It implies that the engine is possible to start automatically if engine friction is improved. These advantages make this engine competitive particularly when it is applied in a small scale DCSP system for converting solar energy into electricity in the mountains or other remote areas where regular maintenance is difficult. Furthermore, in addition to the swinging-to-rotate mode, authors observed other different operating modes of the prototype engine in the experiments, and the physical and geometrical factors affecting the operating modes are still not clear. Unfortunately, no numerical model is available for the dynamic simulation of the start process of the thermal-lag engine. Therefore, in this study a dynamic model is built and incorporated with the thermodynamic model to study the engine start process and clarify the influential factors affecting the operating factors.

The schematic of the thermal-lag Stirling engine is plotted in Fig. 1. The space of the engine is separated into gas chamber, regenerative heater, thermal buffer chamber and compression chamber by the regenerative heater and the piston. As described earlier, the piston is the only one moving part reciprocating between top-dead and bottom-dead points. Therefore, the volumes of gas chamber, regenerative heater chamber and thermal buffer chamber are fixed, whereas the volume of the compression chamber is varied with time. Wall temperatures of the gas chamber and compression chamber (hot part) and the thermal buffer chamber (cold part) are maintained at T_{wg} and T_{wt}, respectively. An axial temperature gradient is hence established within the regenerative heater. The regenerative heater is made of metal wires, screen mesh, or metal foams, which serves not only for heating but also for resulting in a phase angles in the periodic variations of volumes

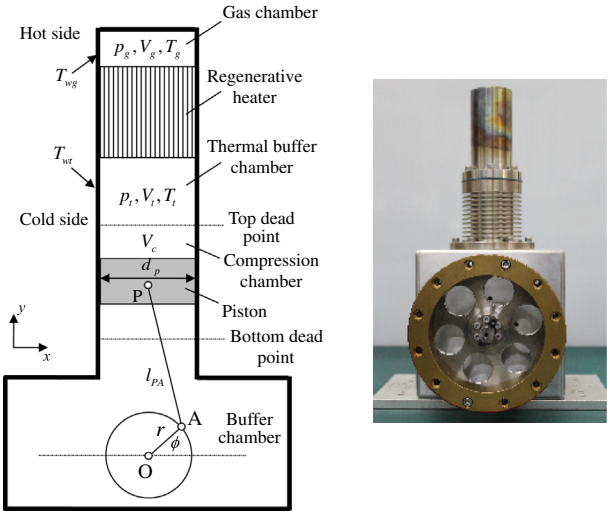

Fig. 1. Schematic of thermal-lag Stirling engine with crank drive mechanism.

Table 1
Geometrical and operating parameters of base-line case.

Geometrical parameters	
r (m)	0.025
l_{PA} (m)	0.075
d_p (m)	0.045
V_t (m^3)	5×10^{-6}
V_g (m^3)	30×10^{-6}
m_p (kg)	0.055
m_{PA} (kg)	0.055
I_{PA} (kg m^3)	5×10^{-5}
I_f (kg m^3)	0.005
Operating parameters	
ω_O^0 (rpm)	500
T_{wt} (K)	300
T_{wg} (K)	1000
R_g (K/W)	1
R_t (K/W)	200
R_c (K/W)	1
$p_0 = p_{b0}$ (Pa)	101,325
μ_p	0.8

and pressures. The prototype engine is regarded as the baseline case in this study. The geometrical and operating parameters of the prototype engine are listed in Table 1. According to experimental observation on the engine, there exist four possible operating modes in the start process:

(1) Rotating mode: the flywheel starts to rotate immediately and the rotation speed smoothly increases to steady-state regime.
(2) Swinging mode: the flywheel exhibits a stable swinging motion but without rotation.
(3) Swinging-to-rotate mode: the flywheel starts with a swinging mode in a short period of time and then proceeds to a uni-directional rotating mode.
(4) Swinging-to-decay mode: the flywheel starts with a swinging mode then the swinging motion gradually decay to a full stop.

The swinging motion is a unique behavior with the thermal-lag Stirling engines, which was also observed by Tailer [16,17]. It is recognized that the operating mode is dependent not only on the geometrical parameters but also on the operating conditions.

2. Dynamic model

In this section, the dynamic model for predicting the dynamic behavior of the thermal-lag Stirling engine is described briefly. The photo of the prototype engine is shown in Fig. 1. The geometric parameters of the thermal-lag Stirling engine with crank drive mechanism are also illustrated in this figure. The crank drive mechanism consists of three parts, namely piston, link, and crank, which is connected to the flywheel. Free body diagrams of the parts are shown in Fig. 2. Pressure force of the working gas is transferred from the piston to the flywheel to push the flywheel rotating. The forces exerted on the parts at any time step can be determined based on force and moment balance principles. Therefore, crank angle, angular speed and acceleration of the flywheel are determined with the help of the dynamic model, and positions, velocities and accelerations of the parts can be readily calculated based on the kinematics analysis [20]. According to the information of positions, velocities and accelerations of the parts, one can determine the volumes of all the chambers in the engine, and then predict the pressures in the chambers for the consecutive time step with the help of the thermodynamic model.

In the dynamic model, the following assumptions are made:

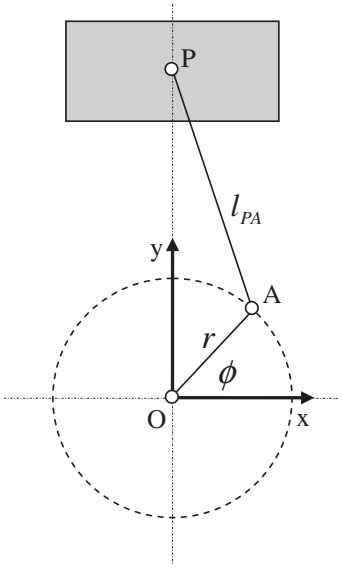

(a) Crank-drive mechanism

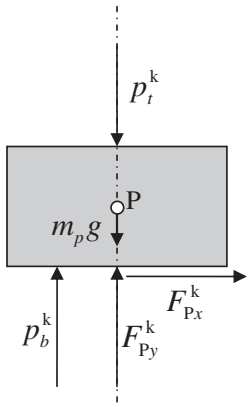

(b) Piston

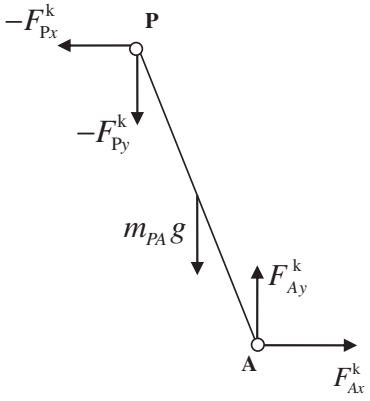

(c) Link PA

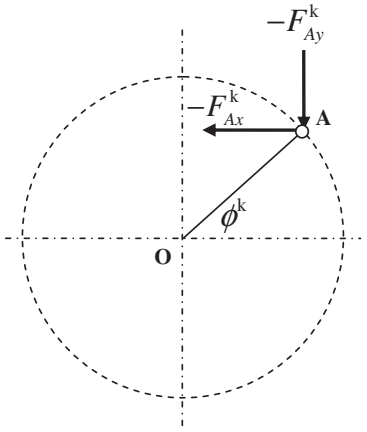

(d) Crank

Fig. 2. Free body diagrams of crank drive mechanism.

1. All moving parts are rigid bodies with no deformation.
2. Magnitude of friction force between the piston and the cylinder is proportional to the normal force to the contact interface.
3. Friction force at each joint is negligible.
4. Center of gravity of each moving part is at its geometric center.

2.1. Velocities and accelerations

In accordance with Fig. 2, the velocity and acceleration of joint A are:

$$\vec{v}_A^k = \vec{\omega}_0^k \times \vec{OA}^k = -\omega_0^k r(\sin\phi^k \vec{i} - \cos\phi^k \vec{j}) \tag{1}$$

$$\begin{aligned}\vec{a}_A^k &= \dot{\vec{\omega}}_0^k \times \vec{OA}^k + \vec{\omega}_0^k \times \left(\vec{\omega}_0^k \times \vec{OA}^k\right) \\ &= -\left[\dot{\omega}_0^k r\sin\phi^k + (\omega_0^k)^2 r\cos\phi^k\right]\vec{i} \\ &\quad + \left[\dot{\omega}_0^k r\cos\phi^k - (\omega_0^k)^2 r\sin\phi^k\right]\vec{j}\end{aligned} \tag{2}$$

where ϕ^k, $\vec{\omega}_0^k = \omega_0^k \vec{k}$, and $\dot{\vec{\omega}}_0^k = \dot{\omega}_0^k \vec{k}$ are crank angle, angular velocity, and angular acceleration, respectively, at time step k in iteration. And, the velocity of piston can be calculated by:

$$\begin{aligned}\vec{v}_P^k &= \vec{v}_A^k + \vec{\omega}_{PA}^k \times \vec{AP}^k \\ &= \left(-\omega_0^k r\sin\phi^k - \omega_{PA}^k e_y^k\right)\vec{i} + \left(\omega_0^k r\cos\phi^k - \omega_{PA}^k e_x^k\right)\vec{j}\end{aligned} \tag{3}$$

where $e_x^k = -r\cos\phi^k$ and $e_y^k = \sqrt{l_{PA}^2 - r^2\cos^2\phi^k}$ representing the x- and y-components of vector $\vec{AP}$. Note that x-component of $\vec{v}_P^k$ is equal to zero. One obtains angular velocity of link PA and y-component of $\vec{v}_P^k$ as

$$\omega_{PA}^k = -\omega_0^k r\sin\phi^k / e_y^k \tag{4}$$

and

$$v_{Py}^k = \omega_0^k r\left(\cos\phi^k - e_x^k \sin\phi^k / e_y^k\right) \tag{5}$$

The acceleration of joint P is determined by

$$\vec{a}_P^k = \vec{a}_A^k + \dot{\vec{\omega}}_{PA}^k \times \vec{AP}^k + \vec{\omega}_{PA}^k \times (\vec{\omega}_{PA}^k \times \vec{AP}^k) \tag{6}$$

Note that x-component of $\vec{a}_{\mathrm{P}}^{\mathrm{k}}$ is equal to zero and $\dot{\omega}_{\mathrm{PA}}^{\mathrm{k}}$ and y-component of $\vec{a}_{\mathrm{P}}^{\mathrm{k}}$ can be expressed as

$$\dot{\omega}_{\mathrm{PA}}^{\mathrm{k}} = -\left[\dot{\omega}_{\mathrm{O}}^{\mathrm{k}} r\sin\phi^{\mathrm{k}} + \left(\omega_{\mathrm{O}}^{\mathrm{k}}\right)^2 r\cos\phi^{\mathrm{k}} + \left(\omega_{\mathrm{PA}}^{\mathrm{k}}\right)^2 e_x^{\mathrm{k}}\right]/e_y^{\mathrm{k}} \tag{7}$$

and

$$a_{\mathrm{Py}}^{\mathrm{k}} = \left[\dot{\omega}_{\mathrm{O}}^{\mathrm{k}} r\cos\phi^{\mathrm{k}} - (\omega_{\mathrm{O}}^{\mathrm{k}})^2 r\sin\phi^{\mathrm{k}} - (\omega_{\mathrm{PA}}^{\mathrm{k}})^2 e_y^{\mathrm{k}}\right] - \left[\dot{\omega}_{\mathrm{O}}^{\mathrm{k}} r\sin\phi^{\mathrm{k}} + \left(\omega_{\mathrm{O}}^{\mathrm{k}}\right)^2 r\cos\phi^{\mathrm{k}} + \left(\omega_{\mathrm{PA}}^{\mathrm{k}}\right)^2 e_x^{\mathrm{k}}\right] e_x^{\mathrm{k}}/e_y^{\mathrm{k}} \tag{8}$$

2.2. Equations of motion

Let $F_{\mathrm{Px}}^{\mathrm{k}}$ and $F_{\mathrm{Py}}^{\mathrm{k}}$ denote the x- and y-components of the force acting on the piston by link PA, and p_t^{k} and p_b^{k} the pressures of the working gas exerted on the top and bottom surfaces of the piston, respectively. One has the equation of motion for the piston as

$$-\pi d_p^2(p_t^{\mathrm{k}} - p_b^{\mathrm{k}})/4 - m_p g + F_{\mathrm{Py}}^{\mathrm{k}} = m_p a_{\mathrm{Py}}^{\mathrm{k}} \tag{9}$$

$F_{\mathrm{Py}}^{\mathrm{k}}$ can be determined by the above equation.

According to force and angular momentum balance, the momentum and the angular momentum equations for link PA can be written as:

$$m_{\mathrm{PA}} a_{\mathrm{PAcg}x}^{\mathrm{k}} = F_{\mathrm{Ax}}^{\mathrm{k}} - F_{\mathrm{Px}}^{\mathrm{k}} \tag{10a}$$

$$m_{\mathrm{PA}} a_{\mathrm{PAcg}y}^{\mathrm{k}} = F_{\mathrm{Ay}}^{\mathrm{k}} - F_{\mathrm{Py}}^{\mathrm{k}} - m_{\mathrm{PA}} g \tag{10b}$$

$$I_{\mathrm{PA}}\dot{\omega}_{\mathrm{PA}}^{\mathrm{k}} = \left(F_{\mathrm{Px}}^{\mathrm{k}} R_y^{\mathrm{k}} - F_{\mathrm{Py}}^{\mathrm{k}} R_x^{\mathrm{k}} + F_{\mathrm{Ax}}^{\mathrm{k}} R_y^{\mathrm{k}} - F_{\mathrm{Ay}}^{\mathrm{k}} R_x^{\mathrm{k}}\right)/2 \tag{11}$$

One can solve Eqs. (10) and (11) for F_{Px}^{k}, F_{Ax}^{k}, and F_{Ay}^{k} and then obtain the torque on joint O as

$$T_{\mathrm{O}}^{\mathrm{k+1}} = r\left(F_{\mathrm{Ax}}^{\mathrm{k}}\sin\phi^{\mathrm{k}} - F_{\mathrm{Ay}}^{\mathrm{k}}\cos\phi^{\mathrm{k}}\right) \tag{12}$$

The angular acceleration of the flywheel $\dot{\omega}_{\mathrm{O}}^{\mathrm{k+1}}$ caused by $\Gamma_{\mathrm{O}}^{\mathrm{k+1}}$, $\Gamma_f^{\mathrm{k+1}}$ and a loading torque $\Gamma_{load}^{\mathrm{k+1}}$ is determined by the equation of angular motion for the flywheel:

$$\dot{\omega}_{\mathrm{O}}^{\mathrm{k+1}} = \left(\Gamma_{\mathrm{O}}^{\mathrm{k+1}} + \Gamma_f^{\mathrm{k+1}} - \Gamma_{load}^{\mathrm{k+1}}\right)/I_f \tag{13}$$

where I_f is moment of inertia of the flywheel, and $\Gamma_{load}^{\mathrm{k+1}}$ is determined by the operating conditions, and $\Gamma_f^{\mathrm{k+1}}$ torque loss due to friction which is calculated by $\Gamma_f^{\mathrm{k+1}} = F_f^{\mathrm{k}} r\cos\phi^{\mathrm{k}}$. F_f^{k} is friction force at the interface between the piston and the cylinder determined by $F_f^{\mathrm{k}} = -\mu_p\left|F_{\mathrm{Px}}^{\mathrm{k}}\right| v_{\mathrm{P}}^{\mathrm{k}}/\left|v_{\mathrm{P}}^{\mathrm{k}}\right|$.

Integrating Eq. (13) with respect to time, one yields the angular velocity and the crank angle at the consecutive time step. As a result, the volumes of the compression and the buffer chambers can be obtained and introduced into the thermodynamic model, which is illustrated in the subsequent section.

The obtained results of the instantaneous crank angle ϕ and angular velocity ω_{O} of the flywheel can be used to estimate the average angular velocity in a cycle as:

$$\omega_{\mathrm{ave}} = \frac{1}{\tau}\oint \omega_{\mathrm{O}}^{\mathrm{k}} dt \tag{14}$$

3. Thermodynamic model

The thermodynamic model presented by Cheng and Yang [19] is extended and is incorporated with the dynamic model. To save the space of the report, the thermodynamic model is described briefly in this section.

In thermodynamic model, some assumptions were made as follows:

(1) Working fluid is air, which is treated as an ideal gas and contained in the engine without leakage.
(2) Pressure inside the engine is uniform.
(3) Wall temperature of the gas chamber is maintained at T_{wg} due to heating by an external high-temperature reservoir, and on the other hand, that of the thermal buffer chamber and the compression chamber is maintained at T_{wt} due to external cooling.
(4) Average flow velocity in the regenerative heater is proportional to the pressure drop.

Herein the gas chamber is called hot side, and the combined space of the thermal buffer chamber and the compression chamber is called cold side. An axial temperature gradient is hence established within the regenerative heater. Mass flow rate through the regenerative heater is determined in terms of the pressure difference between the hot and the cold sides and the properties of the porous medium as well. For a regenerative heater which is composed of metal form or wire-mesh woven-screen matrices, the pressure drop can be expressed in dimensionless form as a Fanning friction factor f [21], which is defined as $f = \frac{D_h}{l_r}\frac{\Delta p}{\rho_{tg}\bar{u}^2}$, where $\Delta p = p_t^{\mathrm{k}} - p_g^{\mathrm{k}}$ and hydraulic diameter $D_h = 4A_r/P$.

The form of the relation between the Fanning friction factor and the Reynolds number corresponding to fully developed laminar flows in micro channels [22] is adopted here as:

$$f\,\mathrm{Re} = K_f \tag{15}$$

where K_f is an empirical coefficient. Relation between average velocity and the pressure drop can then be derived as

$$\bar{u}^{\mathrm{k}} = -D_h^2\left(p_g^{\mathrm{k}} - p_t^{\mathrm{k}}\right)/2\mu K_f l_r \tag{16}$$

The mass flow rate through the regenerative heater can be calculated by $\dot{m}^{\mathrm{k}} = \rho_{tg}^{\mathrm{k}} A_r \bar{u}^{\mathrm{k}}$. The average velocity is assigned to be positive when the working fluid flows from the thermal buffer chamber to the gas chamber.

The axial temperature profile of the regenerative porous matrix is assumed to be a steady and linear function varied from the hot to the cold sides. When the working fluid passes through the regenerative heater, the enthalpy change of the working fluid is mainly caused by the convective heat transfer to or from the working fluid. Therefore,

$$\rho_{tg}^{\mathrm{k}} c_p \bar{u}^{\mathrm{k}} A_r dT = h_r P dx (T_{wr} - T) \tag{17}$$

where T_{wr} is the temperature of the regenerative porous matrix, and P is the cross section void perimeter of the regenerative porous matrix. Since the axial temperature profile of the regenerative porous matrix is assumed to be a steady and linear function varied from T_{wg} to T_{wt}, one has $T_r = -\frac{T_{wt}-T_{wg}}{l_r}x + T_{wt}$. As the working gas flows from the cold to the hot sides, the working gas absorbs heat from the regenerative heater and hence its temperature rises from T_t^{k} to $T_g'^{\mathrm{k}}$. On the contrary, while the working gas flows from the hot to the cold sides, it is cooled and its temperature falls from T_g^{k} to $T_g'^{\mathrm{k}}$. Therefore, the boundary conditions associated with Eq. (17) is described as:

(1) If $\bar{u}^{\mathrm{k}} > 0$, $T = T_t^{\mathrm{k}}$ at $x = 0$:

One obtains the temperature distribution of the working fluid in the regenerative heater as:

$$T(x) = \left(T_t^{\mathrm{k}} - T_{wt}\right)e^{-s^{\mathrm{k}}x} - \frac{T_{wg} - T_{wt}}{l_r}\left(\frac{1 - e^{-s^{\mathrm{k}}x}}{s^{\mathrm{k}}} - x\right) + T_{wt} \tag{18}$$

where $s^{\mathrm{k}} = 4\bar{k}\mathrm{Nu}/\rho_{tg}^{\mathrm{k}} c_p \bar{u}^{\mathrm{k}} D_h^2$, and $\bar{k}$ is thermal conductivity of the working fluid. Let $x = l_r$, and then Eq. (18) gives the temperature of working fluid at the exit of the regenerative heater to the hot side

$$T_g'^{\mathrm{k}} = T_{wg} - \frac{1 - e^{-s^{\mathrm{k}}l_r}}{s^{\mathrm{k}}l_r}(T_{wg} - T_{wt}) + \left(T_t^{\mathrm{k}} - T_{wt}\right)e^{-s^{\mathrm{k}}l_r} \tag{19a}$$

(2) If $\bar{u}^k < 0$, $T = T_g^k$ at $x = 0$:

Similarly, one may obtain the temperature of working fluid at the exit of the regenerative heater to the cold side

$$T_t'^k = T_{wt} + \frac{1 - e^{-s^k l_r}}{s^k l_r}(T_{wg} - T_{wt}) - \left(T_{wg} - T_g^k\right)e^{-s^k l_r} \tag{19b}$$

Transient temperature variation of the working fluid in the cold side (thermal buffer and compression chambers) can be predicted based on the energy conservation law. In finite-difference form, it is expressed as

$$T_t^{k+1} = \frac{m_t^k}{m_t^{k+1}}T_t^k - \frac{p_t^k}{m_t^{k+1}c_v}\left(V_c^{k+1} - V_c^k\right) + \frac{\Delta t}{m_t^{k+1}c_v}\left[\frac{T_{wt} - T_t^k}{R_l^k} - \dot{m}^k c_p\left(f_{tg}^k T_t^k + f_{gt}^k T_t'^k\right)\right] \tag{20}$$

On the right-hand side of the above equation, the second term is the work done by the working fluid, and the first term in bracket denotes the heat transfer which is calculated in terms of thermal resistance and temperature difference. In addition, the second term in the bracket represents energy transfer rate accompanying the mass flow, and hence, it is dependent on the direction of the mass flow. The two direction factors f_{tg}^k and f_{gt}^k appearing in Eq. (20) are introduced to show the direction effect, which are defined as

$$f_{tg}^k = \begin{cases} 1 & if \quad \bar{u}^k > 0 \\ 0 & if \quad \bar{u}^k \leqslant 0 \end{cases}, \quad f_{gt}^k = \begin{cases} 1 & if \quad \bar{u}^k < 0 \\ 0 & if \quad \bar{u}^k \geqslant 0 \end{cases} \tag{21}$$

Similarly, temperature of the working fluid in the cold side (gas chamber) can be calculated by:

$$T_g^{k+1} = \frac{m_g^k}{m_g^{k+1}}T_g^k + \frac{\Delta t}{m_g^{k+1}c_v}\left[\frac{T_{wg} - T_g^k}{R_g} + \dot{m}^k c_p\left(f_{tg}^k T_g'^k + f_{gt}^k T_g^k\right)\right] \tag{22}$$

In Eqs. (20) and (22), R_l and R_g represent the thermal resistances in the cold and the hot sides, respectively. R_l is calculated by [19]

$$R_l^k = \left[\frac{1}{R_t} + \frac{1}{R_c}\left(1 + \frac{l_{PA}}{r} - \sin\phi^k - \sqrt{\left(\frac{l_{PA}}{r}\right)^2 - \cos^2\phi^k}\right)\right]^{-1} \tag{23}$$

There is no moving-boundary work done by the working fluid in the hot side because the volume of the gas chamber is fixed. With the ideal-gas equation of state, the pressures in the cold and the hot sides are calculated, respectively, as

$$p_t^{k+1} = \frac{m_t^{k+1}RT_t^{k+1}}{V_c^{k+1} + V_t} \tag{24a}$$

$$p_g^{k+1} = \frac{m_g^{k+1}RT_g^{k+1}}{V_g} \tag{24b}$$

Total heat input and indicated power can be calculated by:

$$\dot{Q}_{in} = \frac{1}{\tau}\oint \dot{Q}_{t,in}^k + \dot{Q}_{r,in}^k + \dot{Q}_{g,in}^k dt \tag{25a}$$

and

$$\dot{W}_i = \frac{1}{\tau}\oint p_t^k dV_c^k \tag{25b}$$

where $\dot{Q}_{t,in}^k$, $\dot{Q}_{r,in}^k$, and $\dot{Q}_{g,in}^k$ are the heat transfer rates in the thermal buffer chamber, the regenerative heater, and the gas chamber, respectively, and p_t^k is the pressure in the thermal buffer and the compression chambers. In addition, the thermal efficiency (η_t) can be obtained by

$$\eta_t = \dot{W}_i/\dot{Q}_{in} \tag{26}$$

As a loading torque Γ_{load}^k is applied on the engine shaft, the output shaft power of the engine can be yielded by

$$\dot{W}_s = \frac{1}{\tau}\oint \Gamma_{load}^k \omega_O^k dt \tag{27}$$

Thus, the mechanical efficiency (η_m) and the brake thermal efficiency (η_b) can be obtained in terms of the works based on the following definitions:

$$\eta_m = \dot{W}_s/\dot{W}_i \tag{28}$$

and

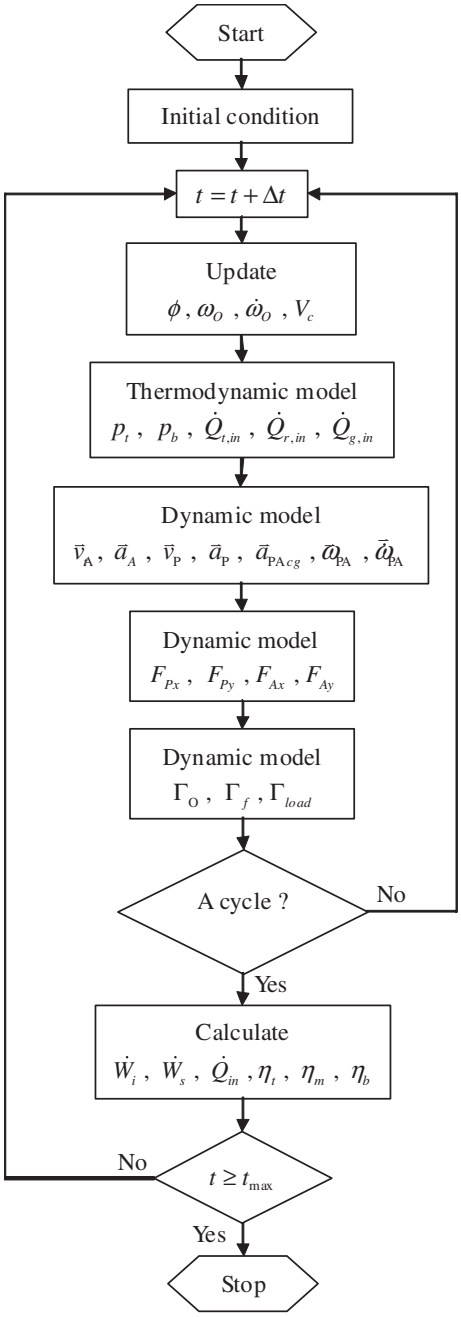

Fig. 3. Flow chart of computation process.

$$\eta_b = \eta_t \eta_m = \dot{W}_s / \dot{Q}_{in} \quad (29)$$

The pressure, the temperature, the instantaneous heat transfer rate and the working gas mass in each of the chambers can be determined with the help of the thermodynamic model. The information of the pressures in the chambers is then introduced to the dynamic model to calculate the crank angle, the angular velocity, and the angular acceleration of the flywheel iteratively. The flow chart of computation process is shown in Fig. 3. As has been described above, the dynamic behavior of thermal-lag Stirling engine can be simulated by combining the dynamic and the thermodynamic models. The geometrical parameters and operating conditions of the baseline case are listed in Table 1. The initial crank angle and angular acceleration are both assigned to be zero. The initial pressures in all the chambers are set to be equal to the atmospheric pressure. The temperatures of the hot and cold parts are maintained at 300 and 1000 K, respectively.

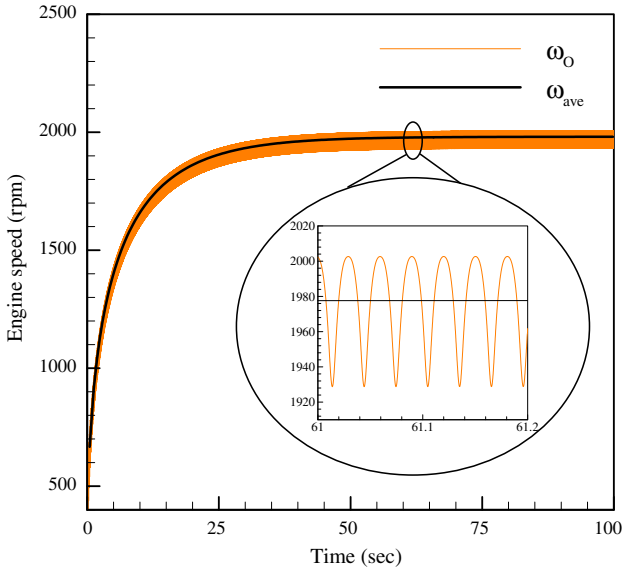

Fig. 4. Instantaneous and average angular velocities.

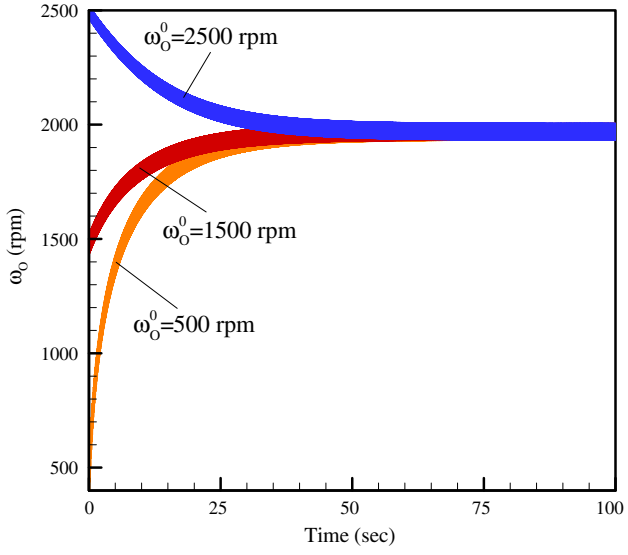

Fig. 5. Instantaneous angular velocity under different initial angular velocities.

4. Results and discussion

For the base-line case, the instantaneous and the cyclic average angular velocities, ω_O and ω_{ave}, are plotted in Fig. 4. The engine speed increases from the initial angular velocity of 500 rpm to steady state regime at 1980 rpm in 100 s, and the fluctuation of instantaneous angular velocity is about 75 rpm. Compared with traditional Stirling engine, the present thermal-lag Stirling engine needs longer time (say, 10 times that with the traditional engines) to reach the steady-state regime. This is because there is no displacer in the thermal-lag Stirling engine to move the working gas immediately. In this regard, it needs more time to adjust the phase between the pressure and the volume variations in working spaces.

Fig. 5 shows the instantaneous angular velocities under different initial angular velocities: $\omega_0^0 = 500$ rpm, $\omega_0^0 = 1500$ rpm, and $\omega_0^0 = 2500$ rpm. It is expected that instantaneous and the cyclic average angular velocities eventually lead to equal cyclic average angular velocity in the steady-state regime. In this figure, all the curves of start processes associated with different initial rotation speeds exhibit smooth changes in the rotation speed from start to steady-state regime. This is called rotating mode in this study.

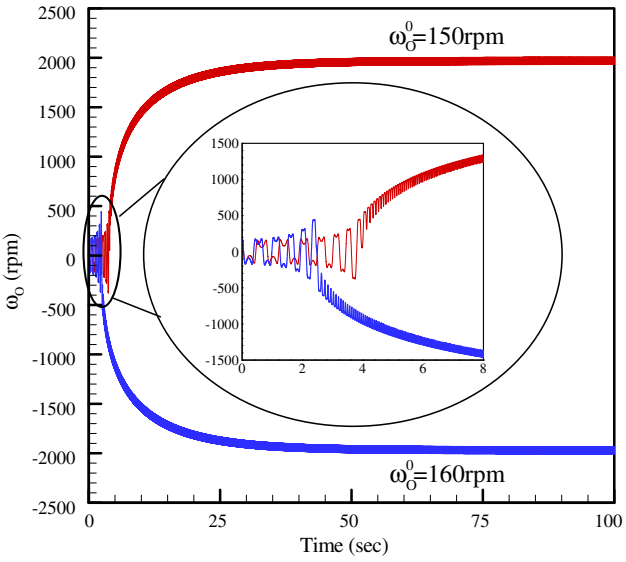

(a) Swinging-to-rotate mode

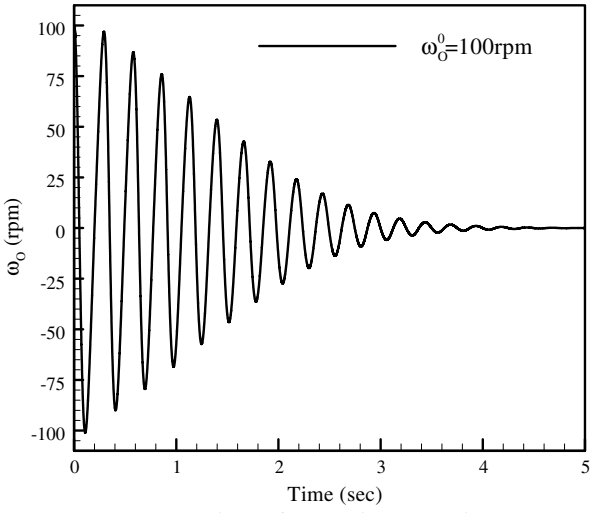

(b) Swing-to-decay mode

Fig. 6. Effects of low initial angular velocity.

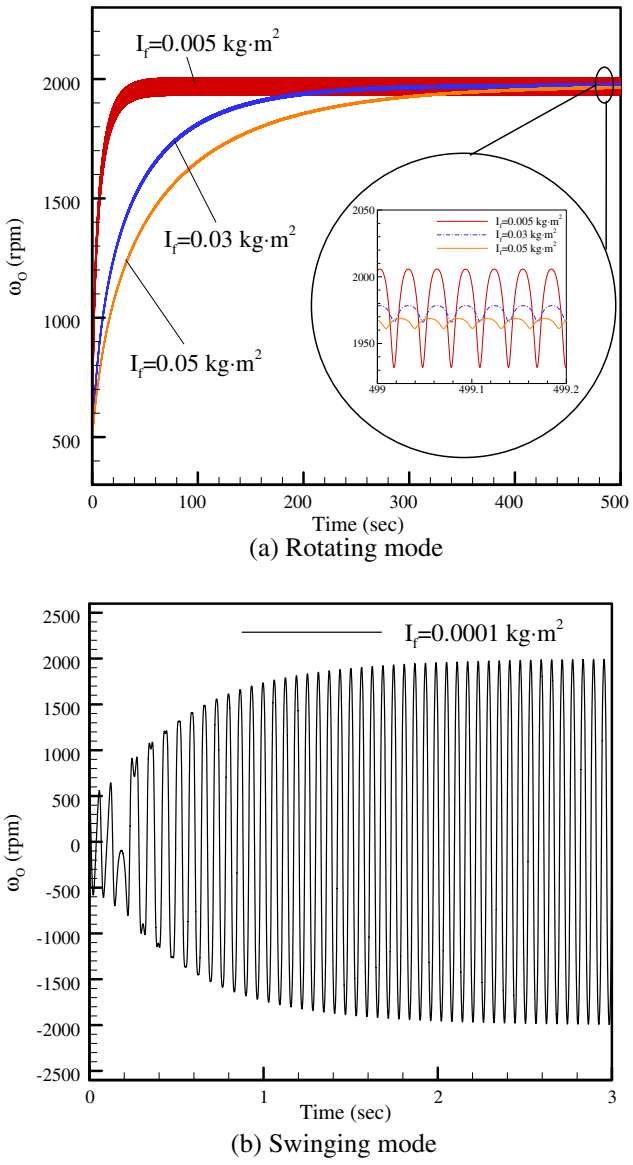

Fig. 7. Effects of moment of inertia of flywheel.

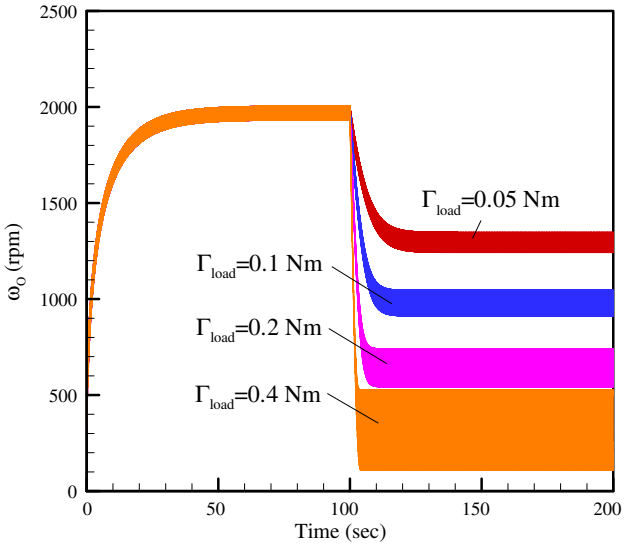

Fig. 8. Instantaneous angular velocity variation under different loading torques.

Fig. 6a shows the instantaneous angular velocities at two initial rotation speeds, 150 and 160 rpm. As the initial angular velocity is lowered, the flywheel swings first till the amplitude of the piston oscillation becomes lager than a half stroke, and then the flywheel starts to rotate randomly in either clockwise or counter-clockwise direction. This is referred to as the swinging-to-rotate mode. It is also found that no matter which direction the flywheel chooses, eventually the magnitude of engine speed will be the same. At a lower initial angular velocity, the flywheel spends longer time in the swinging stage before the steady-state regime is achieved. When the initial angular velocity is further lowered to 145 rpm, the flywheel still starts with a swinging mode; however, the swinging motion gradually decays to a full stop, as illustrated in Fig. 6b. Here one observes the swinging-to-decay mode.

Fig. 7 shows the effects of the moment of inertia of the flywheel on the transient variation in the instantaneous angular velocity. In Fig. 7a, the cases at I_f = 0.005, 0.03, and 0.05 kg m^2 are considered, and the initial angular velocity is fixed at $\omega_0^0 = 500$ rpm. It is seen that the operating mode with all the cases shown in Fig. 7a are rotating mode. With a larger moment of inertia, it takes longer to reach the steady-state regime, and nevertheless the fluctuation of the instantaneous angular velocity is smaller. The average angular velocity in the steady-state regime is independent of the moment of inertia.

When the moment of inertia of flywheel is lowered to 0.0001 kg m^2, it is interesting to find that the angular velocity oscillates stably between positive and negative values, as depicted in Fig. 7b. This actually implies that the flywheel is swinging but not able to rotate. That is called the swinging mode in this study. In the swinging mode, the amplitude of piston oscillation is always less than a half stroke, and thus the engine is unable to turn out to the rotating mode. According to the obtained results, it can be concluded that the operating and geometrical parameters indeed have profound influence on the operating mode of the engine.

Fig. 8 shows the variation in instantaneous angular velocity for the base-line case under different loading torques. The engine is started without loading to the steady-state regime in the first 100 s, and then the loading torque (Γ_{load}) is applied. As a result, the average angular velocity decreases remarkably and attains another steady-state regime. The average angular velocity in the latter steady-state regime is reduced if the loading torque is elevated. It is also observed that the fluctuation of instantaneous angular velocity becomes larger with higher loading torque.

Fig. 9 shows the effects of heating temperature and thermal resistance on shaft power and brake thermal efficiency. In Fig. 9a, the effects of the heating temperature on the performance of the engine at various heating temperatures are evaluated. It is observed the both the shaft power and brake thermal efficiency increase with the heating temperature. At a heating temperature within 800–1200 K, the shaft power reaches a maximum at about 500 rpm. It indicates that the optimal rotation speed of the prototype engine is 500 rpm to gain a maximum power. It is important to mention that the thermal efficiency of the thermal-lag engines are relatively low compared to other types of Stirling engines because with no displacer the working fluid might not be swept effectively between the hot and cold parts. In Fig. 9a, for all cases the brake thermal efficiency is below 14%. Therefore, there is still room to increase the performance of the thermal-lag engines. Fig. 9b conveys the performance of the engine with various thermal resistances. It is clearly observed that to increase the shaft power and the brake thermal efficiency of the engine, the thermal resistances in the hot and the cold parts (R_g and R_c) should be reduced. For the case at $R_g = R_c$ = 0.5 K/W, the maximum shaft power is about 30 W at 1000 rpm. However, at $R_g = R_c$ = 1.0 K/W, the max-

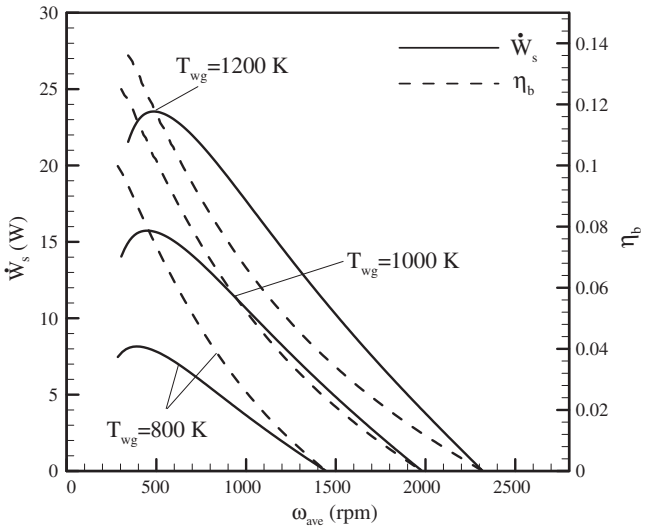

(a) Effect of heating temperature

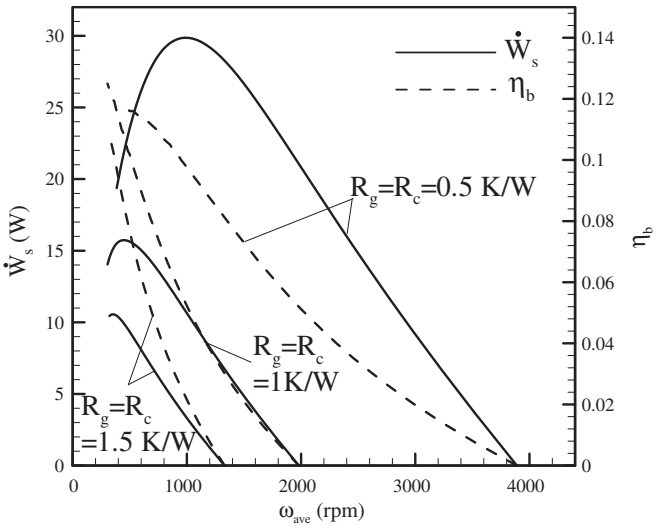

(b) Effect of thermal resistance

Fig. 9. Effects of heating temperature and thermal resistance on shaft power and brake thermal efficiency.

imum shaft power is decreased to 15 W. It is important to mention that if the thermal resistance is too large, the operating mode of the engine may switch from the rotating mode to the undesired swinging-to-decay mode. Fig. 10 shows the results for the case at R_g = - R_c = 10 K/W. In this figure, all other parameters are fixed at the same values as the baseline case except the thermal resistances. The rotation speed is varied from start to the swinging mode at such a higher thermal resistance. This may be attributed to insufficient heat transfers in the hot and cold parts caused by higher thermal resistances.

Effects of stroke and bore size on the shaft power and the brake thermal efficiency are displayed in Fig. 11. The numerical data shown in Fig. 11a indicate that the case with smaller stroke has higher average angular velocity. Nevertheless, with a larger stroke, the compression ratio is higher and heat rejection is more sufficient; therefore, one may have higher shaft power and brake thermal efficiency. Meanwhile, a larger stroke causes larger friction loss. Therefore, there is an optimal stroke for maximum shaft power. In this figure, the optimal stroke is r = 0.03 m and the corresponding maximum shaft power is 16.95 W at 415 rpm. In

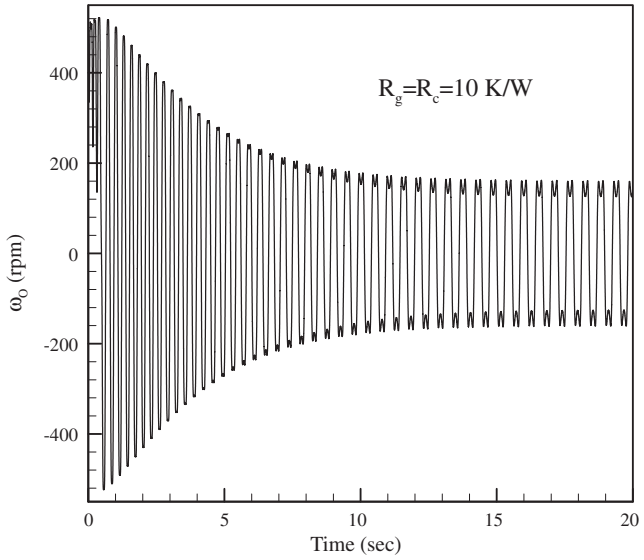

Fig. 10. Rotation speed (from start to swinging mode) at R_g = R_c = 10 K/W.

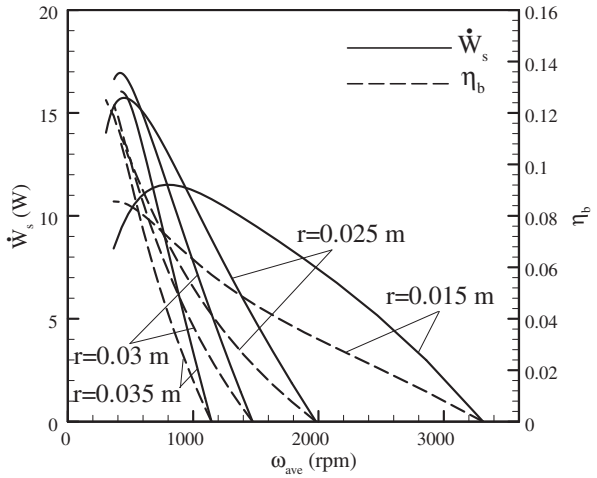

(a) Effect of stroke

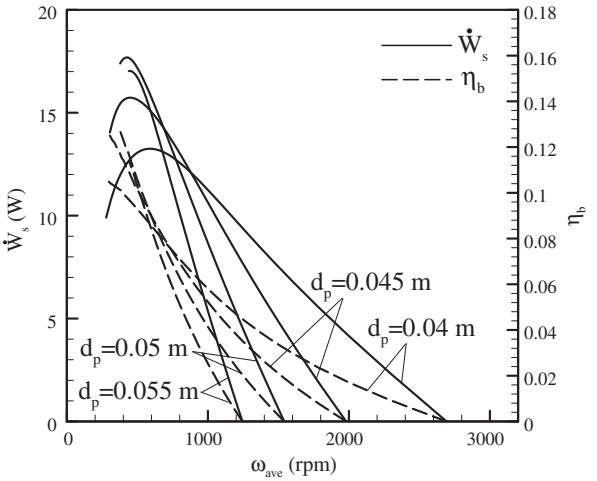

(b) Effect of bore size

Fig. 11. Effects of stroke and bore size on shaft power and brake thermal efficiency.

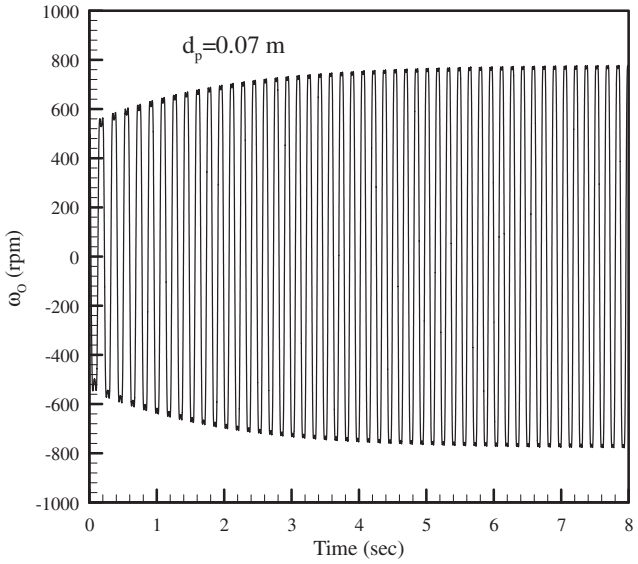

Fig. 12. Rotation speed (from start to swinging mode) at d_p = 0.07 m.

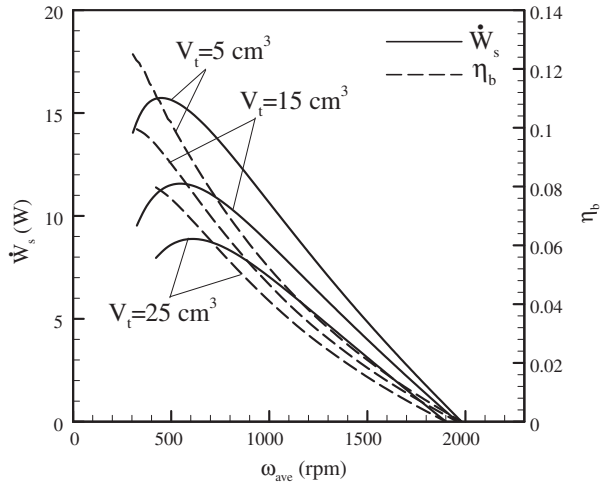

(a) Effect of thermal buffer chamber

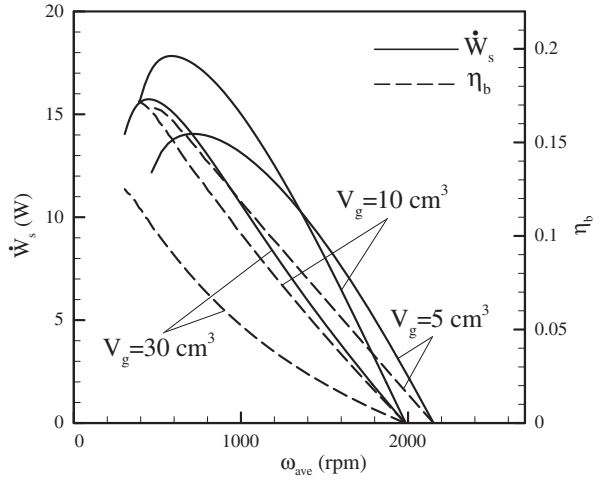

(b) Effect of gas chamber

Fig. 13. Effects of volumes of thermal buffer chamber and gas chamber on shaft power and brake thermal efficiency.

Fig. 11b, the effects of bore size are displayed. It is found that a case with larger bore size has lower average angular velocity and needs a higher initial rotation speed to start the engine. However, on the other hand, with a larger bore size, the cylinder contains more mass of the working gas; therefore, the engine may produce higher shaft power. Hence, one may find an optimal bore size for maximum shaft power. In this figure, it is observed that the optimal bore size is d_p = 0.05 m, and the corresponding maximum shaft power is 17.69 W at 411 rpm.

If the bore size is too large, the engine may switch to the swinging mode or even swinging-to-decay mode. As plotted in Fig. 12, at d_p = 0.07 m, the engine starts from initial instantaneous angular velocity of 500 rpm and eventually attains the swinging mode. In this situation, the flywheel is not able to rotate.

Fig. 13 shows the effects of the volumes of the thermal buffer chamber and gas chamber on the performance of the engine. In Fig. 13a, it is found that a reduction in the volume of the thermal buffer chamber leads to higher performance. This is because the thermal buffer chamber is regarded as a dead space in the thermal-lag Stirling engine which should be minimized. Fig. 13b depicts the performance curves of the engine for various volumes of the gas chamber. It is seen that there exists an optimal gas chamber volume for a maximum shaft power. In this figure, the optimal volume of the gas chamber is found to be V_g = 10 cm^3, and the corresponding maximum shaft power is 17.8 W at 587 rpm. However, if a maximum brake thermal efficiency is of interests, the optimal volume of the gas chamber would be V_g = 5 cm^3.

5. Conclusions

Numerical dynamic simulation of the thermal-lag Stirling engines by incorporating a dynamic model with a thermodynamic model has been performed. In the simulation, different operating modes, including rotating mode, swinging mode, swinging-to-rotate mode, and swinging-to-decay mode, have been observed. The rotating mode is desired and can be achieved if the operating and geometrical parameters are properly selected. In a poor design, the engine may switch to the swinging or even the swinging-to-decay mode. For the particular cases considered here, the swinging mode is observed for the cases with a larger bore size (d_p = 0.07 m) or larger thermal resistances ($R_g = R_c$ = 10 K/W).

It is found that the brake thermal efficiency of the engine is monotonically reduced by increasing engine speed. However, parametric study of the dependence of the shaft power of the engine speed shows that there exists a maximum value of the shaft power at an optimal operating engine speed. There also exist optimal stroke, bore size, and volume of gas chamber for achieving maximum shaft power or higher brake thermal efficiency. Through the parametric study for the baseline case, it has been found that the optimal stroke is r = 0.03 m, optimal bore size d_p = 0.05 m, and optimal volume of the gas chamber V_g = 10 cm^3.

References

[1] Mancini TR, Heller P, Butler B, Osborn B, Schiel W, Goldberg V, et al. Dish-Stirling systems: an overview of development and status. J Sol Energy Eng 2003;125(2):135–51.
[2] Mancini TR. Solar-electric dish stirling system development. In: Proceedings of the 4th European Stirling forum 1998, Osnabruck, Germany; 1998.
[3] Ruelas J, Velazquez N, Cerezo J. A mathematical model to develop a Scheffler-type solar concentrator coupled with a Stirling engine. Appl Energy 2013;101:253–60.
[4] Lombardi K, Ugursal VI, Beausoleil-Morrison I. Proposed improvements to a model for characterizing the electrical and thermal energy performance of Stirling engine micro-cogeneration devices based upon experimental observations. Appl Energy 2010;87(10):3271–82.

[5] Parente A, Galletti C, Riccardi J, Schiavetti M, Tognotti L. Experimental and numerical investigation of a micro-CHP flameless unit. Appl Energy 2012;89(1):203–14.
[6] Thombare DG, Verma SK. Technological development in the Stirling cycle engines. Renew Sustain Energy Rev 2008;12(1):1–38.
[7] Cheng CH, Yang HS. Optimization of geometrical parameters for Stirling engines based on theoretical analysis. Appl Energy 2012;92:395–405.
[8] Rochelle P, Grosu L. Analytical solutions and optimization of the exo-irreversible schmidt cycle with imperfect regeneration for the three classical types of Stirling engine. Oil Gas Sci Technol 2011;66(5):747–58.
[9] Ceperley PH. A pistonless Stirling engine–the traveling wave heat engine. J Acoust Soc Am 1979;66:1508–13.
[10] Swift GW. Thermoacoustic engines. J Acoust Soc Am 1988;84:1145–80.
[11] Swift GW. Analysis and performance of a large thermoacoustic engine. J Acoust Soc Am 1992;92:1551.
[12] Swift GW, Garrett SL. Thermoacoustics: a unifying perspective for some engines and refrigerators. J Acoust Soc Am 2003;113:2379.
[13] Hamaguchi K, Ushijima Y, Hiratsuka Y. Basic characteristics of pulse tube engine. In: Proceedings of the 12th international stirling engine conference, Duraham Univ, UK; 2005. p. 275–84.
[14] Yoshida T, Yazaki T, Futaki H, Hamaguchi K, Biwa T. Work flux density measurements in a pulse tube engine. Appl Phys Lett 2009;95(4):044101.
[15] Chen NCJ, West CD. A single-cylinder valveless heat engine. In: Proceedings of the intersociety energy conversion engineering conference, Philadelphia, USA, August 10–14, 1987.
[16] Tailer PL. External combustion Otto cycle thermal lag engine. Proc Intersoc Energy Convers Eng Conf 1993;1:943–7.
[17] Tailer PL. Thermal lag test engines evaluated and compared to equivalent Stirling engines. Proc Intersoc Energy Convers Eng Conf 1995;3:353–7.
[18] Arques P. Theoretical and numerical study, improvement of the Wicks-Tailer cycle. Proc Intersoc Energy Convers Eng Conf 1995;3:407–12.
[19] Cheng CH, Yang HS. Theoretical model for predicting thermodynamic behavior of thermal-lag Stirling engine. Energy 2013;49(1):218–28.
[20] Shames IH. Engineering mechanics: dynamics. Prentice-Hall; 1966.
[21] Dukhan N. Correlations for the pressure drop for flow through metal foam. Exp Fluids 2006;41(4):665–72.
[22] Shah RK, London AL. laminar flow forced convection in ducts: a source book for compact heat exchanger analytical data. New York: Academic press; 1978.